INORGANIC CHEMISTRY FRONTIERS

RESEARCH ARTICLE

View Article Online
View Journal | View Issue

Cite this: *Inorg. Chem. Front.*, 2025, **12**, 8513

Expanding NIR-IIc nanothermometry: architectural control of Tm^{3+}-doped $NaGdF_4$ core/shell nanoparticles

Nan Liu, † Hana Mirmajidi, Lucas Crozier and Eva Hemmer *

Received 25th July 2025,
Accepted 14th September 2025

DOI: 10.1039/d5qi01571e

rsc.li/frontiers-inorganic

Near-infrared (NIR) nanothermometers are promising for biomedical applications due to reduced optical scattering and absorption of NIR light that matches the biological transparency windows when compared to UV or visible light. Yet, the exploration of nanothermometers that operate in the NIR-IIc (1700–1880 nm) and NIR-III (2080–2340 nm) spectral regions remains scarce. To address this gap, we propose a series of Tm^{3+}-, Er^{3+}-, and Yb^{3+} doped $NaGdF_4$ core/shell/shell nanoparticles dispersed in toluene for double-band ratiometric nanothermometry operating in the NIR-IIc region. The influence of the doping concentration of activator and sensitizer ions Tm^{3+} and Yb^{3+} on the Er^{3+} and Tm^{3+} emissions has been systematically investigated. The maximal S_r value based on the Tm^{3+} $^3F_4 \rightarrow {}^3H_6$ (1850 nm) and Er^{3+} $^4I_{13/2} \rightarrow {}^4I_{15/2}$ (1550 nm) radiative transitions reached values as high as 2.3% $°C^{-1}$ at 50 °C. This is significantly higher than previously reported S_r values, particularly for ratiometric NIR nanothermometers. To further explore the even longer wavelengths, Tm^{3+} and Ho^{3+} co-doped $NaGdF_4$ core/shell nanoparticles were designed, exhibiting emissions at 1850 nm (Tm^{3+}) and 2000 nm (Ho^{3+}) reaching the NIR-III window and a maximum S_r value of 0.58% $°C^{-1}$ (T = 20 °C). These findings contribute to the establishment of design principles and a library of sought-after novel NIR optical thermal nanosensors.

Introduction

In recent years, luminescent nanothermometry has attracted growing interest for potential application in different fields, including microfluidics, microelectronics, and biomedicine,[1–4] due to its remote and minimally invasive thermal sensing capabilities.[5,6] Luminescent nanothermometry is a spectroscopic technique for temperature measurements based on the temperature-associated changes in the optical properties of a suitable probe.[7,8] Among luminescent nanothermometers, those that operate in the near-infrared (NIR) spectral region have shown particular potential for biomedical applications. In contrast to UV/visible light, NIR light exhibits lower phototoxicity and deeper penetration into biological tissue due to reduced optical scattering and absorption.[9] While there is no clear consensus about the definition, the NIR spectral region is commonly subdivided into several biological optical transparency windows.[10,11] Conventionally, the region from 700 to 950 nm was defined as NIR-I, that from 1000 to 1350 nm as NIR-II, and the spectral region from 1550 to 1870 nm was referred to as NIR-III. Much less explored is the 4th biological window, NIR-IV, that covers the 2050–2400 nm spectral region.[12]

Interestingly, recent work by Feng *et al.* proposes the redefinition of the biological windows and optimal spectral regions for optical bioimaging.[13] Moderate light absorption by water in the spectral region around 1450 nm was found to positively contribute to intravital imaging. The collection of light within this spectral region was identified as a recommendable option, when using probes the emission of which is strong enough to resist the partial absorption loss. Consequently, the NIR windows were proposed as follows (a notation that will be adopted throughout this work): NIR-I: 750–900 nm, NIR-II: 900–1880 nm, and NIR-III: 2080–2340 nm. Herein, the NIR-II window was suggested to be subdivided into so-called NIR-IIx (1400–1500 nm) and NIR-IIc (1700–1880 nm).[13]

To date, various types of materials have been reported for the design of luminescent nanothermometers that operate in the NIR spectral region, including organic compounds, quantum dots, transition metal-doped oxides, and lanthanide (Ln^{3+})-based nanoparticles (Ln-NPs).[14,15] Among these, Ln-NPs have been widely investigated due to their excellent photostability, relatively low toxicity, and NIR emission under NIR excitation that perfectly aligns with above-defined biological

Department of Chemistry and Biomolecular Sciences, University of Ottawa, Ottawa, ON, K1N 6N5, Canada. E-mail: ehemmer@uottawa.ca
† Current affiliation: Hubei Key Laboratory of Drug Synthesis and Optimization, Jingchu University of Technology, Jingmen, Hubei, 448000, PR China.

windows.[12,16] As a result, over the past decade, significant progress has been made in the development of a large variety of potential nanothermometers for biomedical applications.[17–28] The working principle of most of these nanothermometers is based on a ratiometric approach using the luminescence intensity ratio (LIR) between spectrally distant emission bands.[29] Herein, advantage is taken of the NIR emission of Ln^{3+} ions like Nd^{3+} (880 nm, 1060 nm, 1340 nm),[21,24,25,27,28] Ho^{3+} (1180 nm),[30] Pr^{3+} (1300 nm),[31] Tm^{3+} (800 nm, 1470 nm, 1800 nm),[19,26,32] and Er^{3+} (1550 nm).[22,23,33] However, the exploration of optical probes that emit at wavelengths longer than 1600 nm and into the NIR-IIc and NIR-III spectral regions remains scarce. This is surprising given the increasing awareness of challenges related to the reliability of ratiometric thermal sensing that relies on calibration curves.[34,35] These challenges include spectral distortion as a function of the environment of the optical probes – an issue that was reported to be less severe when shifting towards longer wavelengths.[36]

One notable example is a study by Nexha *et al.* from 2020.[37] Herein, the authors report a ratiometric thermometer based on Tm^{3+} and Ho^{3+} co-doped $KLu(WO_4)_2$ crystalline powders with an average particle size of approximately 150 nm. The different temperature-dependence of the observed emission intensities at 1800 nm ($^3F_4 \rightarrow {}^3H_6$ radiative transition of Tm^{3+}) and 1960 nm ($^5I_7 \rightarrow {}^5I_8$ radiative transition of Ho^{3+}) resulted in a thermometer with a maximum relative thermal sensitivity (S_r) of 0.9% °C^{-1} at 20 °C. This constitutes the first proof-of-concept for Ln-based nanothermometry in the NIR-IIc spectral region. Though, biomedical applications often require dispersible nanomaterials of homogenous morphology and narrow size distribution. Addressing this challenge, Li *et al.* reported a NIR nanothermometer based on $NaErF_4/NaYF_4$:Tm^{3+} core/shell NPs dispersed in toluene, a first step towards applications that require solvent dispersibility.[38] The authors explored the temperature-dependent LIR between the NIR emissions of Er^{3+} (1550 nm) and Tm^{3+} (1800 nm) corresponding to their $^4I_{13/2} \rightarrow {}^4I_{15/2}$ and $^3F_4 \rightarrow {}^3H_6$ transitions, respectively, and reported a maximum S_r value of 0.61% °C^{-1} at 30 °C. In 2024, our group reported Pr^{3+}/Ho^{3+}-doped $NaGdF_4$ core/shell/shell (CSS) NPs as nanothermometers operating in the 1200–1300 nm spectral region.[31] By comparing the thermometric performances of various Pr^{3+}/Ho^{3+}-based NP architectures, it was found that the separation of the Ln^{3+} emitters in different layers was required for controlled energy transfer between the Ln^{3+} ions, ultimately allowing for improved thermometric performance. The promising nanothermometers reported by Nexha *et al.*[37] and Li *et al.*[38] now motivate the rational design of core/(multi-)shell Ln-NPs of compositions optimized for the operation in the NIR-IIc and into the NIR-III beyond 2000 nm spectral regions, whereas not only S_r, the quantitative parameter used to assess and compare the thermal sensing performance of different nanothermometers, but also other key performance metrics, such as uncertainty and repeatability, shall be assessed. Therefore, we here propose a series of novel Ln-NPs with optimized temperature-dependent photoluminescence for nanothermometry in the NIR-IIc spectral region.

First, a series of Tm^{3+}-, Er^{3+}-, and Yb^{3+}-doped $NaGdF_4$ core/multi-shell NPs, dispersible in toluene, was synthesized by microwave-assisted synthesis, and the nanoparticles' NIR-II luminescence under 980 nm excitation was systematically investigated. Herein, the focus was set on the architectural design, assessing the impact of the doping concentration of activator and sensitizer ions Tm^{3+} and Yb^{3+} on the Er^{3+} and Tm^{3+} emissions centered at 1550 and 1850 nm, respectively. The LIR of the two emission bands was found to be highly temperature-dependent, resulting in a maximum S_r value of 2.3% °C^{-1} at 50 °C, which is significantly larger than previously reported S_r values, particularly for ratiometric NIR nanothermometers.[38] To take advantage of even longer wavelengths, we further investigated the thermometric performance of Tm^{3+} and Ho^{3+} co-doped $NaGdF_4$ core/shell NPs dispersed in toluene, exhibiting emission bands centered at 1850 and *ca.* 2000 nm. Herein, the use of Tm^{3+} is of particular interest as allowing for excitation at 808 nm, reducing potential excitation laser-induced heating effects that might be observed upon 980 nm excitation. Though not being on par with the performance of the Er^{3+}- and Tm^{3+}-based nanothermometer, the maximum S_r of 0.58% °C^{-1} obtained at 20 °C identifies the monodispersed Tm^{3+}- and Ho^{3+}-doped NPs as suitable candidates that fully operate in the NIR-IIc spectral region. These findings contribute to the establishment of a library of sought-after novel NIR optical thermal sensors.

Results and discussion

NIR-IIc emitting Er^{3+}, Tm^{3+}, Yb^{3+} co-doped core/shell/shell nanoparticles (Er/Tm- and Er/Yb,Tm-CSS NPs)

Synthesis and structural characterization. A series of oleate (OA)-capped core/shell/shell (CSS) β-$NaGdF_4$ NPs co-doped with Yb^{3+}, Er^{3+}, and Tm^{3+} were synthesized using the microwave-assisted approach previously established by our group (see Experimental section and SI for details).[39] For optimization of the NIR luminescence and thermometric performance, a total of three different CSS architectures was designed. One type of CSS-NPs consisted of a 2 mol% Er^{3+} and 20 mol% Yb^{3+} co-doped core and an inner shell that was co-doped with 20 mol% Yb^{3+} and either 10 or 20 mol% of Tm^{3+}. An outer undoped $NaGdF_4$ shell was added to protect the optically active Ln^{3+} ions in the core and inner shell from surface quenching. This resulted in $NaGdF_4$:Er^{3+}(2 mol%), Yb^{3+}(20 mol%)/$NaGdF_4$:Tm(x mol%),Yb^{3+}(20 mol%)/$NaGdF_4$ CSS-NPs with x = 10 and 20, respectively, hereafter referred to as Er/Yb,$Tm^{10\%}$-CSS and Er/Yb,$Tm^{20\%}$-CSS NPs, respectively. The rather high concentrations of Tm^{3+} ions were chosen based on previously published reports showing intense NIR-IIc emission at *ca.* 1800 nm.[12,40] The variation between 10 and 20 mol%, allowed to investigate the effect of the Tm^{3+} dopant concentration on (i) the NIR-IIc emission of the Tm^{3+} ion and (ii) the performance of the CSS-NPs as thermal sensors. Co-

doping of the inner shell with Yb^{3+} was expected to promote Yb^{3+}-enabled energy migration between the core and shell region of the CSS-NPs, potentially influencing the thermometric performance. To confirm this hypothesis, the third CSS architecture consisted of the same core composition (*i.e.*, $NaGdF_4$ co-doped with 2 mol% of Er^{3+} and 20 mol% of Yb^{3+}), but the inner shell was singly doped with 20 mol% of Tm^{3+}, lacking the additional Yb^{3+} co-dopant. Again, an outer undoped $NaGdF_4$ shell was added to protect the optically active Ln^{3+} ions in the core and inner shell from surface quenching. The resultant $NaGdF_4$:Er^{3+}(2 mol%), Yb^{3+}(20 mol%)/$NaGdF_4$:Tm(20 mol%)/$NaGdF_4$ CSS NPs are hereafter labelled as Er/$Tm^{20\%}$-CSS NPs. An overview of all Yb^{3+}, Er^{3+}, and Tm^{3+} co-doped CSS NPs, including their composition, size, and sample name is provided in Table S1.

X-ray diffraction (XRD) analysis confirmed that all CSS-NPs crystallized in the hexagonal β-phase of $NaGdF_4$ (space group: $P6_3/m$) (Fig. S1). The morphology and size of the NPs was examined using transmission electron microscopy (TEM). The TEM images of the OA-capped Er/Tm- and Er/Yb,Tm-CSS NPs and their respective size distributions are shown in Fig. 1 (see Fig. S2 for additional TEM analysis of the respective core and CS-NPs). All NPs were monodisperse with narrow size distributions. The core NPs exhibited a spherical morphology with an average size between 6.2 and 6.6 nm (Fig. S2A1, B1 and C1 as well as size distribution plots in Fig. 1). Growing a Yb^{3+} and Tm^{3+} co-doped shell resulted in CS-NPs of *ca.* 12–14 nm (12.6 ± 1.1 nm and 14.0 ± 1.5 nm), with comparable shell thicknesses of *ca.* 3–4 nm (Fig. S2A2, B2 and Fig. 1B, D). Further growth of a *ca.* 3.5 nm undoped $NaGdF_4$ shell led to overall CSS-NP sizes of 19.3 ± 1.9 nm and 21.0 ± 1.9 nm for Er/Yb, $Tm^{10\%}$-CSS and Er/Yb,$Tm^{20\%}$-CSS, respectively (Fig. 1A–D). Upon growth, the NPs adopted a quasi-spherical morphology starting to form hexagon-like structures, which is ascribed to the intrinsic crystallographic properties of the hexagonal phase of $NaGdF_4$.[41] As shown in Fig. 1E, F and Fig. S2C, samples with only Tm^{3+} in the inner shell, *i.e.*, Er/$Tm^{20\%}$-CSS NPs, were of comparable dimensions. The Tm^{3+} doped inner shell was *ca.* 2.3 nm thick, whereas the outer shell had a thickness of *ca.* 3.8 nm, overall resulting in a CSS-NP size of 18.4 ± 1.5 nm. Some decrease in inner shell thickness was noticeable upon lack of Yb^{3+} doping in the inner shell (*ca.* 2.3 *versus* 3.4 nm). This observation is in line with previous studies reporting effects of Ln^{3+} dopant choice and concentration on particle growth.[42] All CSS-NPs retained a quasi-spherical shape.

Optical properties of Er/Tm- and Er/Yb,Tm-CSS NPs. The downshifting photoluminescence properties of the obtained Er/Tm- and Er/Yb,Tm-CSS NPs, dispersed in toluene, were investigated under 980 nm excitation. As shown in Fig. 2A, at

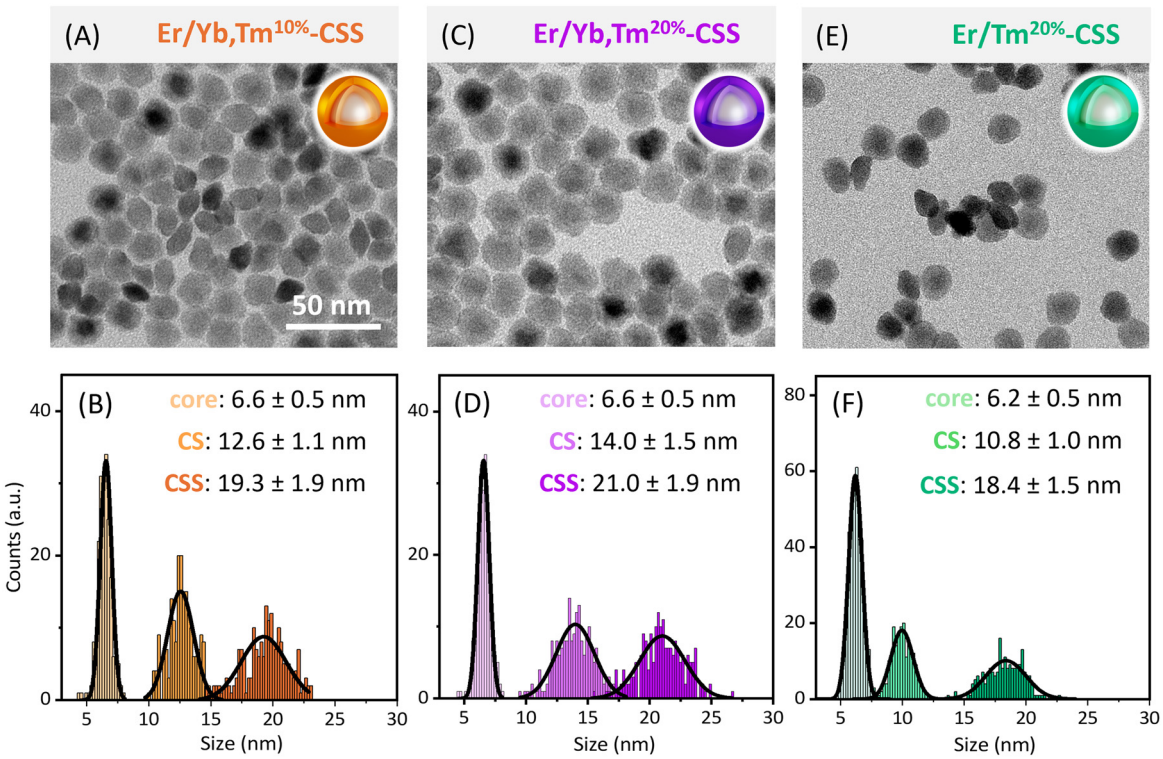

Fig. 1 (A, C and E) TEM images of the Er/Yb,Tm- and Er/Tm-CSS NPs. All of these CSS NPs consisted of a core doped with 2 mol% Er^{3+} and 20 mol% Yb^{3+}. The inner shell was doped with (A) 10 mol% Tm^{3+} and 20 mol% Yb^{3+} (Er/Yb,$Tm^{10\%}$), (C) 20 mol% Tm^{3+} and 20% Yb^{3+} (Er/Yb,$Tm^{20\%}$), and (E) 20 mol% Tm^{3+} (Er/$Tm^{20\%}$), respectively. An undoped outer shell was added to all compositions to form the CSS-NPs. The 50 nm scale bar applies to all TEM images. (B, D and F) The corresponding size distributions of the Er/Yb,Tm- and Er/Tm-CSS NPs and their respective core as well as CS-NPs. The numbers in (B, D and F) are the average particle size ± standard deviation.

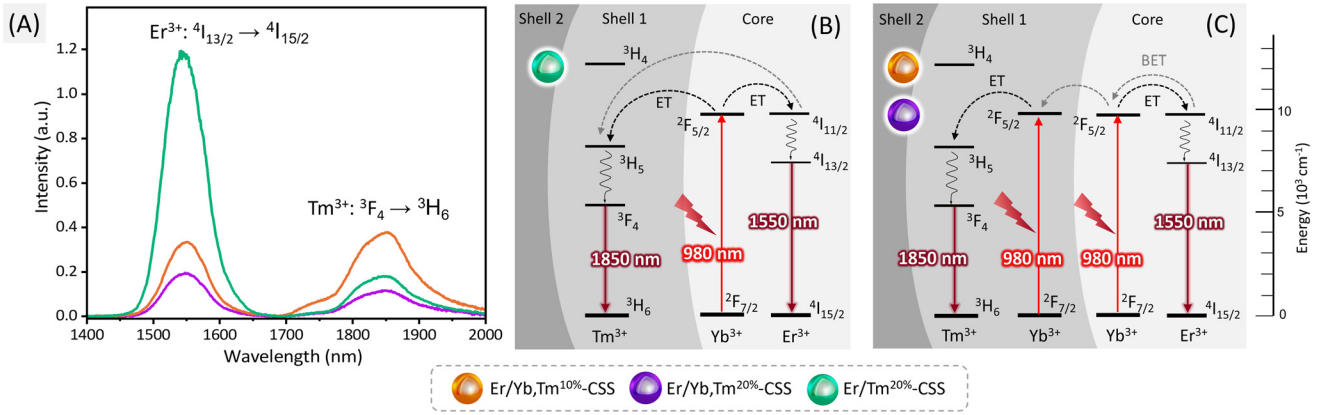

Fig. 2 (A) Room temperature NIR emission spectra of Er/Yb,Tm- (orange and purple sample) and Er/Tm-CSS (green sample) NPs as a function of their architecture. Excitation wavelength: 980 nm; laser power density: 6.7 W cm^{-2}; CSS-NP concentration: 10 mg mL^{-1} in toluene. Energy transfer diagram for CSS-NPs with (B) 20 mol% of Tm^{3+} as single dopant as well as (C) 10 or 20 mol% of Tm^{3+} co-doped with Yb^{3+} in the inner shell (shell 1), highlighting the Er^{3+} and Tm^{3+} ions' NIR emission. The outer shell (shell 2) was undoped. Solid straight arrows indicate excitation and emission, wavey arrows indicate non-radiative decay, and dashed arrows indicate energy (ET) as well as back energy (BET) transfer. See Fig. S3B–D for energy level diagrams including upconversion.

room temperature, all samples exhibited the expected photoluminescence in the NIR spectral region. The well-studied emission of Er^{3+}, centred at 1550 nm (NIR-II, formerly categorized as NIR-III), corresponds to the ion's $^4I_{13/2} \rightarrow {}^4I_{15/2}$ radiative f–f transition.[22] In addition, the emission peak at 1850 nm is ascribed to the Tm^{3+} $^3F_4 \rightarrow {}^3H_6$ radiative f–f transition, overlapping with the NIR-IIc spectral region.[13,37]

Among the three samples, Er/$Tm^{20\%}$-CSS NPs (colour code: green) exhibited the most intense Er^{3+} NIR emission. Moreover, their Er^{3+} emission intensity was significantly stronger than that of their Tm^{3+} emission. This resulted in a Tm^{3+}-to-Er^{3+} intensity ratio (I_{Tm}/I_{Er}), based on the integrated areas of the respective emission bands, of only 0.23. This can be attributed to the resonance of the energy levels of the Yb^{3+} sensitizer ($^2F_{5/2}$) and the Er^{3+} ($^4I_{11/2}$) activator ion, both doped into the core, leading to efficient energy transfer from Yb^{3+} to Er^{3+} upon 980 nm excitation. Consequently, the population of the emitting Er^{3+} level ($^4I_{13/2}$) and the subsequent emission are favoured (Fig. 2B). Conversely, energy transfer from the Yb^{3+} sensitizer to the Tm^{3+} activator is less efficient due to the energetic mismatch between the Yb^{3+} $^2F_{5/2}$ and Tm^{3+} $^3H_5$ levels. The $Yb^{3+} \rightarrow Tm^{3+}$ energy transfer is further hampered (though not suppressed) as Tm^{3+} and Yb^{3+} ions were doped into different regions of the CSS architecture (core *versus* inner shell).

Remarkably, the Er/Yb,$Tm^{10\%}$-CSS sample (sample code: orange) showed the strongest Tm^{3+} NIR emission among all the samples (Fig. 2A). This is the result of the more efficient Yb^{3+}-activated excitation of the Tm^{3+} ion. More precisely, the population of the Tm^{3+} ions' $^3H_5$ level is fostered by the closer distance between the Yb^{3+} and Tm^{3+} ions, both co-doped into the inner shell. Following non-radiative decay to the $^3F_4$ level, radiative decay to the $^3H_4$ ground level takes place (Fig. 2C). In parallel, the presence of Yb^{3+} in the core and the inner shell in this architecture can foster Yb^{3+} mediated energy migration from the core to the inner shell. This can depopulate the Yb^{3+} excited states in the core, thus, hampering efficient Er^{3+} excitation. Consequently, the Er^{3+} NIR emission is lower for Er/Yb, $Tm^{10\%}$-CSS NPs in comparison to that of Er/$Tm^{20\%}$-CSS NPs. Overall, this comes along with a relatively large Tm^{3+}-to-Er^{3+} intensity ratio (I_{Tm}/I_{Er}) of 1.80.

Upon increase of the Tm^{3+} dopant concentration from 10 to 20 mol% (Er/Yb,$Tm^{20\%}$-CSS, sample code: purple), the Tm^{3+} emission decreased. Tm^{3+} is prone for cross-relaxation and self-quenching processes, which is fostered by the high concentration of Tm^{3+}, ultimately leading to the loss of emission intensity.[43] In addition, the emission intensity of the Er^{3+} NIR band decreased upon increase of the Tm^{3+} concentration in the inner shell. This might be explained by a more pronounced energy transfer from the excited level of the Yb^{3+} (and Er^{3+}) ions in the core towards Tm^{3+} ions in the inner shell as the number of neighbouring Tm^{3+} ions increased. This depopulation of the Yb^{3+} sensitizer ion's and the Er^{3+} activator ion's excited states *via* energy transfer to the $^3H_5$ Tm^{3+} level can then result in the reduced Er^{3+} NIR emission intensity. On the other hand, this energy migration may be expected to result in a relative emission enhancement of the Tm^{3+} NIR emission ($^3F_4 \rightarrow {}^3H_6$) for Er/Yb,$Tm^{20\%}$-CSS NPs (purple sample) compared to Er/Yb,$Tm^{10\%}$-CSS NPs (orange sample). However, for Er/Yb,$Tm^{20\%}$-CSS NPs, the I_{Tm}/I_{Er} ratio was 1.06 opposed to 1.80 for Er/Yb,$Tm^{10\%}$-CSS NPS, indicating that Tm^{3+} cross-relaxation and self-quenching processes were dominant, ultimately hampering more efficient Tm^{3+} NIR emission.

The assessment of the upconversion (UC) spectra can provide additional insight into the excitation and emission pathways of the Er/Yb,Tm- and Er/Tm-CSS NPs (Fig. S3). Under excitation with 980 nm light, Er/$Tm^{20\%}$-CSS NPs (green sample) exhibited significantly brighter upconverted Er^{3+} emission than the Er/Yb,Tm-CSS NPs (orange and purple sample) (Fig. S3). As discussed above, the lack of Yb^{3+} as co-dopant in

the inner shell reduces depopulation of the excited $^4I_{11/2}$ level of the Er^{3+} ion as hampering energy migration from the core to the inner shell. Consequently, more efficient UC to the green ($^2H_{11/2}$, $^4S_{3/2}$) and red ($^4F_{9/2}$) emitting Er^{3+} levels can take place.

As expected, given the high Tm^{3+} dopant concentration of 10 and 20 mol%, respectively, the UC spectra of all CSS NPs lack the characteristic blue emission of Tm^{3+} ions (Fig. S3A). Only negligible UC intensity was detected at *ca.* 700 nm for Er/$Tm^{20\%}$-CSS NPs (green sample, Fig. S3A and B). Though, interestingly, relatively strong UC emission at *ca.* 800 nm, ascribed to the $^3H_4 \rightarrow {}^3H_6$ Tm^{3+} transition, was observed for Er/Yb,$Tm^{10\%}$-CSS NPs (Fig. S3A and C, orange sample). Er/Yb,$Tm^{20\%}$-CSS NPs (purple sample) exhibited the second strongest Tm^{3+} UC emission at *ca.* 800 nm, likely weakened due to concentration-induced quenching process (Fig. S3A and D). The lack of Yb^{3+} in the inner shell (Er/Tm-CSS NPs, green sample) resulted in an inefficient UC process leading to low intensities for this $^3H_4 \rightarrow {}^3H_6$ Tm^{3+} transition (Fig. S3A and B).

To further corroborate the proposed energy transfer mechanisms leading to the observed trends in NIR emission, photoluminescence decay curves and the corresponding lifetimes of the Er^{3+}, Tm^{3+}, and Yb^{3+} NIR emissions for the Er/Tm- and Er/Yb,Tm-CSS NPs were determined. Data and a brief discussion are provided in the Fig. S4.

Double-band ratiometric thermometric performance of the Er/Tm-and Er/Yb,Tm-CSS NPs

Encouraged by the Er^{3+} and Tm^{3+} emissions within the NIR-II spectral region, including the NIR-IIc window, the thermal sensing capability of the Er/Tm- and Er/Yb,Tm-CSS NPs was assessed, seeking the potential for nanothermometry in the underexplored spectral region beyond 1500 nm. The thermometric performance of the samples was evaluated by temperature-dependent photoluminescence spectroscopy on their dispersions in toluene (NP concentration: 10 mg mL^{-1}). Prior to assessing their thermometric performance, potential laser-induced heating effects had to be ruled out. Therefore, power-dependent irradiation of the pure solvent, *i.e.*, toluene, with the 980 nm laser diode was conducted. Only a small temperature increase of 0.3 °C, 0.5 °C, and 0.7 °C was observed at power densities of 3.0 W cm^{-2}, 5.3 W cm^{-2}, and 6.7 W cm^{-2}, respectively, after 5 min of laser irradiation (Fig. S5). Subsequently, photoluminescence spectra of the Er/Yb,$Tm^{20\%}$-CSS NPs (the weakest emitter, Fig. 2A) were recorded at different power densities in order to determine the lowest excitation power density possible still allowing for sufficient emission intensity, while minimizing heating effects. Based on the spectra shown in (Fig. S6), a laser power density of 6.7 W cm^{-2} was chosen for all subsequent temperature-dependent photoluminescence measurements.

As shown in Fig. 3A–C, irrespective of the CSS architecture, elevating the temperature from 20 to 50 °C resulted in a decrease in the intensity of the Er^{3+} emission at 1550 nm. Such thermally induced quenching effect was also observed in other Er^{3+}-based materials and has been ascribed to the increased dissipation of excitation energy at elevated temperatures, which may result from the prevalence of non-radiative relaxations (*e.g.*, multiphonon relaxation) and the depopulation of the $^4I_{13/2}$ excited state of the Er^{3+} ion.[23,44] Conversely, the intensity of the Tm^{3+} emission at 1850 nm increased with rising temperature, likely due to the increased probability of phonon-assisted energy transfer from Yb^{3+} ($^2F_5$) to Tm^{3+} ($^3H_5$).[45]

Comparing the various CSS architectures, the temperature-induced increase of the Tm^{3+} emission was more pronounced upon co-doping of the inner shell with Yb^{3+}, *i.e.*, for Er/Yb,$Tm^{10\%}$-CSS and Er/Yb,$Tm^{20\%}$-CSS NPs (Fig. 3A and B, orange and purple sample) than for Er/$Tm^{20\%}$-CSS NPs (Fig. 3C, green sample). Hence, co-doping of the inner shell with Yb^{3+} ions does not only enhance the Tm^{3+} emission due to closer vicinity of the sensitizing Yb^{3+} ions to the activating Tm^{3+} ions. It also renders the Tm^{3+} emission more sensitive to temperature changes given that the $Yb^{3+} \rightarrow Tm^{3+}$ energy transfer is phonon-assisted.

Most interestingly, the different intensity changes for the Er^{3+} and Tm^{3+} emission bands as a function of temperature allowed for an all-optical temperature readout *via* a double-band ratiometric approach. Therefore, the thermometric parameter, *i.e.*, the luminescence intensity ratio (LIR = I_{Tm}/I_{Er}) was calculated between two integration regions, I_{Tm} (1700–2000 nm) and I_{Er} (1400–1700 nm) (see SI for details and equations used to calculate the thermometric parameters).[46] Fig. 3D summarizes the LIR values obtained for all Er/Tm- and Er/Yb,Tm-CSS samples, following an exponential temperature dependence in the temperature range from 20 to 50 °C. The thermometric performance of the CSS NPs was assessed by comparing their relative thermal sensitivity, S_r, which correlates the change of the LIR with the temperature variation. Among the three explored CSS architectures, Er/Yb,$Tm^{10\%}$-CSS NPs exhibited the highest maximum S_r value of 2.32 ± 0.13% $°C^{-1}$ at 50 °C (Fig. 3E). Maximum S_r values for the other CSS NPs were 1.58 ± 0.21% $°C^{-1}$ at 50 °C for Er/Yb,$Tm^{20\%}$-CSS NPs as well as 1.56 ± 0.21% $°C^{-1}$ at 20 °C for Er/$Tm^{20\%}$-CSS NPs. Over the assessed temperature range, all of the determined S_r values were above the 1% $°C^{-1}$ threshold (S_r values for NIR nanothermometers are typically smaller than 1% $°C^{-1}$), deeming them good performers for double-band ratiometric thermal sensing.[34,47] Noteworthy, all maximum S_r values obtained were significantly higher than the previously reported value for $NaErF_4/NaYF_4$:Tm^{3+} NPs (0.61% $°C^{-1}$ at 30 °C).[38] While the authors also designed a core/shell architecture to separate Er^{3+} and Tm^{3+} ions, key differences between the previously published and the here presented Ln-NPs are the dopant concentration, the lack of Yb^{3+}, and the direct excitation of Tm^{3+} using 800 nm light. This resulted in the enhancement of the Er^{3+} emission and weakening of the Tm^{3+} emission at increasing temperature – a trend opposite to that observed in our CSS NPs. This demonstrates how the careful design of the NP architecture contributes to the optimization of the thermometric behaviour.

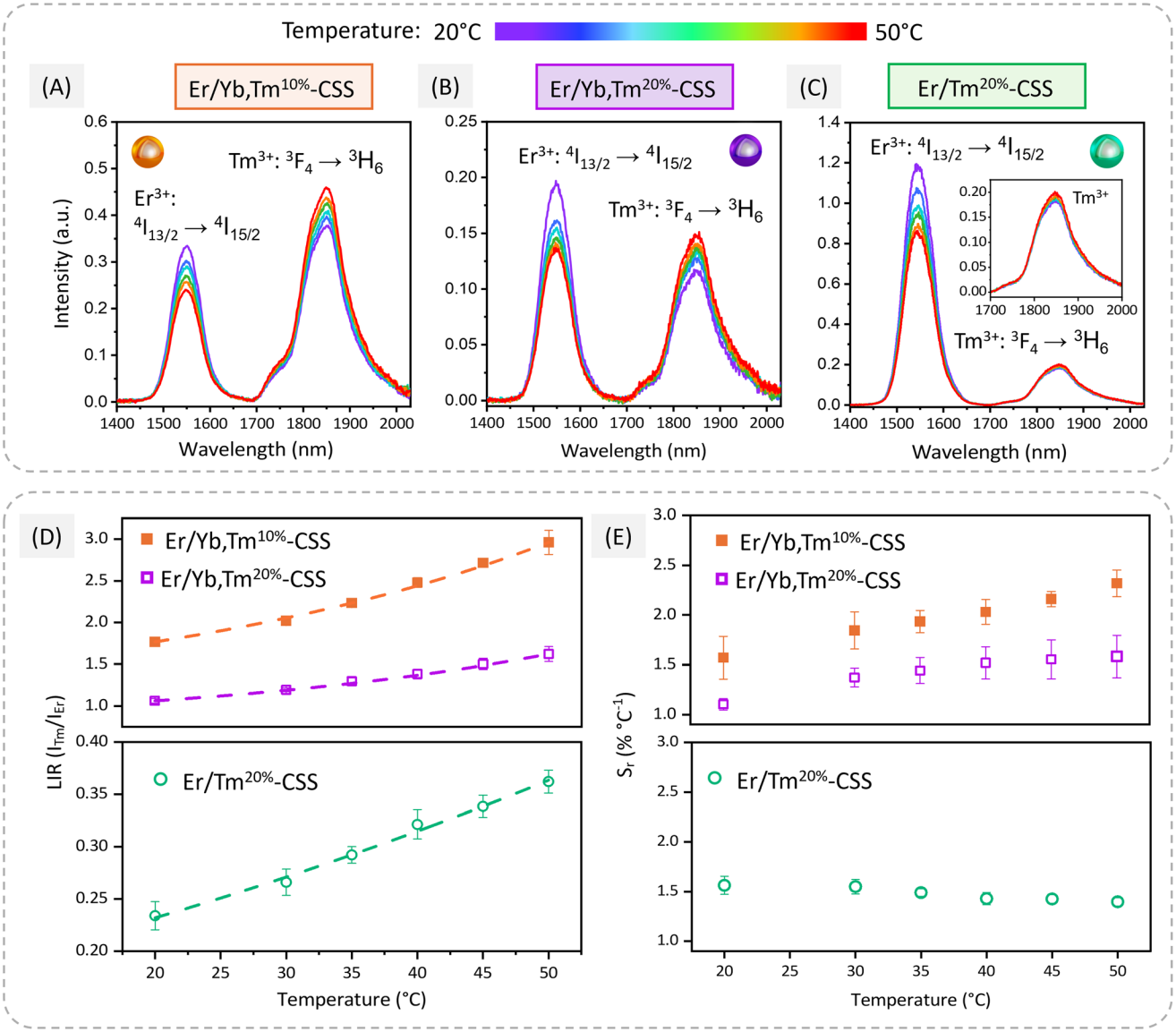

Fig. 3 Double-band ratiometric nanothermometry with OA-capped Er/Tm- and Er/Yb,Tm-CSS NPs dispersed in toluene (10 mg mL^{-1}). Temperature-dependent NIR emission spectra recorded on (A) Er/Yb,$Tm^{10\%}$-CSS, (B) Er/Yb,$Tm^{20\%}$-CSS, and (C) Er/$Tm^{20\%}$-CSS NPs. Excitation wavelength: 980 nm; laser power density: 6.7 W cm^{-2}. (D) Temperature dependence of the LIR (I_{Tm}/I_{Er}) defined for the Tm^{3+} $^3F_4 \rightarrow {}^3H_6$ and Er^{3+} $^4I_{13/2} \rightarrow {}^4I_{15/2}$ radiative transitions. The dashed lines are exponential fits. (E) Relative thermal sensitivities (S_r) as a function of temperature. Data points in (D) and (E) are average values based on independent measurements performed on three aliquots taken from the same stock dispersion. Error bars are the associated standard deviation.

By comparing the S_r value in light of the three different CSS architectures, the following key aspects could be identified for the establishment of design principles. First, the addition of Yb^{3+} as co-dopant was advantageous with respect to higher S_r values, especially within the physiologically relevant temperature range. Revisiting the NIR photoluminescence spectra (Fig. 2A), for the best performing CSS architecture, *i.e.*, Er/Yb, $Tm^{10\%}$-CSS NPs, the presence of Yb^{3+} led to an increase in the intensity of the Tm^{3+} emission and a decrease of the Er^{3+} emission, bringing both emission bands on par. In addition, the Tm^{3+} band exhibited a stronger temperature-dependence due to facilitated phonon-assisted $Yb^{3+} \rightarrow Tm^{3+}$ energy transfer processes (Fig. 3A, B *versus* Fig. 3C). Conversely, lower S_r values were obtained for the CSS architecture that showed significantly lower intensity as well as temperature dependence of the Tm^{3+} band. Second, for Er/Yb,Tm-CSS NPs, the Tm^{3+} dopant concentration effected the thermometric performance, with 20 mol% of Tm^{3+} leading to worse performance than 10 mol% of Tm^{3+}. This correlated with the weaker Tm^{3+} emission (in absolute terms and relative to the Er^{3+} emission). Lastly, Er/$Tm^{20\%}$-CSS NPs represented a distinct case for which S_r was found to be the least affected by temperature, showing a rather constant value of *ca.* 1.5% $°C^{-1}$ over the investigated temperature range. A slightly thicker outer shell (*ca.* 3.8 nm)

might contribute to this behaviour, as previously observed for Pr^{3+}- and Ho^{3+}-based CS NPs.[47]

Besides S_r, two additional key performance metrics, *i.e.*, temperature uncertainty (δT) and reproducibility of the measurement (R), were assessed. The δT is the smallest temperature change that can be detected in a given measurement and is mainly determined by the signal-to-noise ratio during the spectral acquisition.[46] The δT values were in the range of 0.33 to 0.45, 0.45 to 0.76, and 0.33 to 0.49 °C for Er/Yb,$Tm^{10\%}$-CSS, Er/Yb,$Tm^{20\%}$-CSS, and Er/$Tm^{20\%}$-CSS NPs, respectively (Fig. S7). All of these values are below 1 °C under the given measurement conditions, indicating a good temperature resolution of the Er/Tm- and Er/Yb,Tm-CSS NPs, whereas Er/Yb,$Tm^{10\%}$-CSS NPs exhibited the lowest average value and smallest associated standard deviation. To assess the reproducibility of the thermometric behaviour, three independent measurements were performed on three aliquots taken from the same stock dispersion, and values of *ca.* 95% were found for all samples (Fig. S8).

Considering all three thermometric parameters, *i.e.*, S_r, δT, and R, Er/Yb,$Tm^{10\%}$-CSS NPs exhibited the best thermal performance among the studied CSS architectures. Optimization of the CSS architecture allowed to finetune the NPs' structure–property relationships, leading to significant higher S_r values than previously reported for Er/Tm based nanothermometers that operate in the spectral region beyond 1500 nm, while retaining good uncertainty and reproducibility, indicating its potential as NIR-IIc nanothermometer.

Ho^{3+} and Tm^{3+} co-doped nanoparticles (Ho,Tm-CS NPs): leveraging emissions at the 2000 nm spectral region

Synthesis and structural characterization. In order to explore NIR-nanothermometers operating in an even longer NIR wavelength region (NIR-III) and under 808 nm excitation, Ho,Tm-based NPs were designed. With the Tm^{3+} emission centred at *ca.* 1850 nm and the Ho^{3+} emission centred at *ca.* 2000 nm, an optical probe was obtained that operates in the NIR-IIc (1700–1880 nm) and reaches into the NIR-III (2050–2400 nm) windows. Inspired by the reported study of Tm^{3+} and Ho^{3+} co-doped $KLu(WO_4)_2$,[37] we synthesized two types of Tm^{3+}- and Ho^{3+}-containing core/shell NPs (hereafter Ho,Tm-CS NPs), aiming to obtain homogenous NPs with a narrow size distribution for the evaluation of their thermometric performance in dispersion. Both CS samples constituted of a $NaGdF_4$ core doped with 1 mol% Ho^{3+} and different concentrations of Tm^{3+}, *i.e.*, 10 or 15 mol%. An undoped $NaGdF_4$ shell was added to enhance emission, resulting in $NaGdF_4$:Ho(1%),Tm(x %)/$NaGdF_4$ CS NPs (x = 10 or 15), hereafter labelled as Ho,$Tm^{10\%}$-CS and Ho,$Tm^{15\%}$-CS, respectively. XRD analysis confirmed that the NPs crystallized in the hexagonal β-phase of $NaGdF_4$ (Fig. S9). Based on TEM analysis, the NPs were monodisperse with a narrow size distribution and of comparable dimensions (Fig. S10 and Table S1). The core sizes of the Ho,$Tm^{10\%}$-CS and Ho,$Tm^{15\%}$-CS NPs were 5.0 ± 0.2 nm and 6.1 ± 0.3 nm, respectively. Growing an undoped $NaGdF_4$ shell resulted in CS-NPs of 11.9 ± 0.9 nm and 11.6 ± 0.8 nm with shell thicknesses of 3.5 nm and 2.8 nm, respectively.

Optical properties of Ho,Tm-CS NPs. In the proposed Ho,Tm-CS NP architectures, the Tm^{3+} ions were used not only as emitters but also as sensitizers, absorbing the excitation energy from the 808 nm light source. As shown in Fig. 4A, under 808 nm excitation, both Ho,Tm-CS NPs exhibited down-shifting luminescence with emission maxima at 1850 nm (Tm^{3+}) and 1980 nm (Ho^{3+}). The partial energy level diagrams of Tm^{3+} and Ho^{3+} are depicted in Fig. 4B. Accordingly, upon absorption of a photon at 808 nm, Tm^{3+} is promoted from its $^3H_6$ ground state to the $^3H_4$ excited state, followed by non-radiative decay down to the $^3F_4$ state. From the $^3F_4$ state, the emission of 1850 nm is generated by radiative decay to the ground state. In the presence of Ho^{3+} ions, an energy transfer (ET) process can take place from the $^3F_4$ level of Tm^{3+} to the $^5I_7$ level of Ho^{3+}, due to the energy resonance of these two states.[48] Following the population of the excited Ho^{3+} level, radiative decay to the ground state leads to the characteristic Ho^{3+} emission at 1980 nm. Alternatively, the emitting Ho^{3+} level can be populated by ET from the $^3H_4$ Tm^{3+} to the $^5I_5$ Ho^{3+} level, followed by non-radiative decay to $^5I_7$.[49] Upon increase of the Tm^{3+} concentration from 10 mol% to 15 mol%, the emission intensity of Tm^{3+} increased (Fig. 4A), which can be ascribed to enhanced cross-relaxation (CR) processes, such as ($^3H_6$, $^3H_4$) ↔ ($^3F_4$, $^3F_4$), at higher Tm^{3+} dopant concentrations (Fig. 4B).[48,50] This is in line with the shorter lifetime of the Tm^{3+} $^3F_4$ excited state for Ho,$Tm^{15\%}$-CS NPs (*ca.* 332 μs) compared to that of Ho,$Tm^{10\%}$-CS NPs (*ca.* 581 μs) (Fig. S11A).[51] The intensity of the Ho^{3+} emission band decreased upon increase of the Tm^{3+} dopant concentration (Fig. 4A). This might be explained by favoured back-energy transfer (BET) processes from Ho^{3+} to Tm^{3+} ions, thus, further contributing to the enhancement of the Tm^{3+} emission at 1850 nm, while leading to the reduced Ho^{3+} emission at *ca.* 2000 nm. This is supported by the observed shortening of the lifetime of the Ho^{3+} $^5I_7$ excited state upon increase of the Tm^{3+} dopant concentration from *ca.* 656 μs for Ho,$Tm^{10\%}$-CS to *ca.* 377 μs for Ho,$Tm^{15\%}$-CS NPs (Fig. S11B).

Double-band ratiometric thermometric performance of Ho,Tm-CS NPs

The thermometric performance of the Ho,Tm-CS NPs was evaluated by temperature-dependent photoluminescence spectroscopy on their dispersions in toluene (10 mg mL^{-1}). As shown in Fig. 4C and D, the emission intensities of Tm^{3+} and Ho^{3+} both increased with elevating temperature from 20 to 50 °C. Such thermally induced increase is related to the increased probability of phonon-assisted, non-radiative processes leading to the quenching of the excited Tm^{3+} state ($^3H_4$, $^3H_5$) down to the emitting Tm^{3+} state ($^3F_4$).[51] This increases the population of the Tm^{3+} emitting level as well as the resonant Ho^{3+} level ($^5I_7$), hence, leading to an overall increase in luminescence intensity. To assess the thermometric performance, the values for the LIR between the Tm^{3+} (I_{Tm}: 1700–1900 nm) and the Ho^{3+} (I_{Ho}: 1900–2200 nm) emission

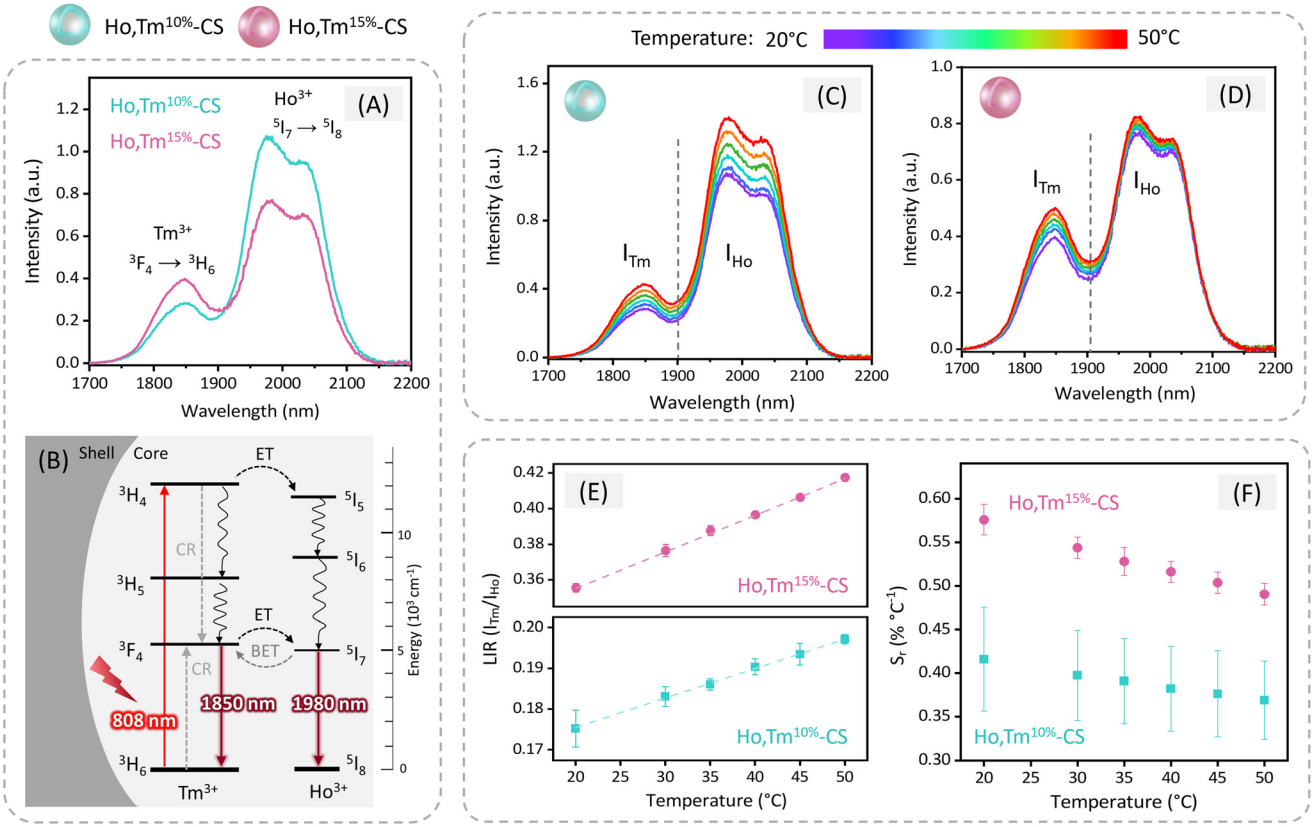

Fig. 4 (A) Room temperature NIR emission spectra of OA-capped Ho,Tm$^{10\%}$-CS (cyan) and Ho,Tm$^{15\%}$-CS (pink) NPs. (B) Partial energy diagram of Tm^{3+} and Ho^{3+}, including excitation, energy transfer (ET), back energy transfer (BET), cross relaxation (CR), and emission pathways in Ho,Tm-CS NPs. Temperature-dependent NIR emission spectra recorded on (C) Ho,Tm$^{10\%}$-CS and (D) Ho,Tm$^{15\%}$-CS NPs. Excitation wavelength: 808 nm; laser power density: 13.3 W cm^{-2}; NP concentration: 10 mg mL^{-1} in toluene. (E) Temperature dependence of the LIR (I_{Tm}/I_{Ho}) defined for the Tm^{3+} $^3F_4 \rightarrow {}^3H_6$ and Ho^{3+} $^5I_7 \rightarrow {}^5I_8$ radiative transitions. The dashed lines are linear fits. (F) Relative thermal sensitivities (S_r) as a function of temperature. Data points in (E) and (F) are average values based on triplicates, and error bars are the associated standard deviation.

(LIR = I_{Tm}/I_{Ho},) were determined as a function of the dispersions' temperature. For both samples, the LIR values increased linearly with temperature (Fig. 4E), being indicative for a more pronounced enhancement of the Tm^{3+} emission than the Ho^{3+} emission. This phenomenon suggests that increasing temperature favours BET processes from Ho^{3+} to Tm^{3+} ions and/or cross-relaxation processes fostering the population of the emitting $^3F_4$ level of Tm^{3+}. Maximum S_r values for Ho,Tm$^{10\%}$-CS and Ho,Tm$^{15\%}$-CS samples were 0.42 ± 0.06% °C^{-1} and 0.58 ± 0.02% °C^{-1} at 20 °C, respectively. In line with the above identified design principles, the sample for which the emission bands used for the ratiometric approach were of more comparable intensities, *i.e.*, Ho,Tm$^{15\%}$-CS NPs, showed a better thermometric performance. In addition, the slightly thinner outer shell is likely to contribute to the higher S_r value. These S_r values are slightly lower than the value reported for Ho,Tm-doped $KLu(WO_4)_2$ powders (*ca.* 0.9% C^{-1} at 20 °C).[37] However, to the best of our knowledge, this is the first Ho,Tm-based example for nanothermometry at this spectral region operating in dispersion.

The nanothermometers exhibited δT values that ranged from 0.9 to 1.2 °C for Ho,Tm$^{10\%}$-CS NPs and from 0.6 to 0.8 °C for Ho,Tm$^{15\%}$-CS NPs (Fig. S12). In line with the higher S_r value, this points towards a slightly better performance in case of Ho,Tm$^{15\%}$-CS NPs. Conducting heating–cooling cycles, the repeatability of the nanothermometers was assessed. The R values of both Ho,Tm-CS NPs were determined to be higher than 97% (Fig. S13), demonstrating good repeatability of the thermometric sensing capability. Consequently, though the Ho,Tm-CS NPs exhibited overall lower S_r values than the Er/Tm- and Er/Yb,Tm-CSS NPs, the designed Ho,Tm-CS nanothermometers provide a stepping stone for further exploration of solvent dispersible nanothermometers operating in the NIR-IIc and NIR-III range.

Conclusions

In conclusion, core/(multi-)shell Tm^{3+}-doped $NaGdF_4$ NPs co-doped with either Er^{3+} and Yb^{3+} or Ho^{3+} were successfully designed for ratiometric optical thermal sensing in the NIR-II (including NIR-IIc) and NIR-III spectral region in the 20–50 °C temperature range. Importantly, the wet-chemical approach for the synthesis of the nanothermometers using a microwave-

assisted strategy allowed for the dispersibility of the NPs in solvents, *i.e.*, toluene, a prerequisite for many potential applications. Under 980 nm excitation of the Er/Tm- and Er/Yb,Tm-CSS NPs, emissions of Tm^{3+} (1850 nm) and Er^{3+} (1550 nm) corresponding to their $^3F_4 \rightarrow {}^3H_6$ and $^4I_{13/2} \rightarrow {}^4I_{15/2}$ radiative transitions were found to strongly depend on temperature. Herein, the influence of the Tm^{3+} dopant concentrations and co-doping with Yb^{3+} were assessed. As a result, following a double-band ratiometric approach based on the integrated Tm^{3+} and Er^{3+} emission bands, Er/Yb,$Tm^{10\%}$-CSS NPs exhibited S_r values from 1.57 to 2.32% $°C^{-1}$ in the investigated temperature range. This constitutes a significant improvement of the thermal sensing capability when compared to previously reported Er/Tm-based nanothermometers operating in this spectral region, while retaining good uncertainty and reproducibility. In addition, the thermometric performance of Ho,Tm-based NPs in toluene was investigated to explore their potential at even longer wavelengths. Tm^{3+} allowed for excitation with 808 nm, and the maximum S_r value was determined as 0.58% $°C^{-1}$ at 20 °C. Herein, the use Ho^{3+} is of particular interest as its emission due to the $^5I_7 \rightarrow {}^5I_8$ f–f transition reaches beyond 2000 nm, opening the NIR-III biological window. While it remains difficult to obtain the NIR-IIc and NIR-III emission in water, this demonstration of NIR-IIc/NIR-III nanothermometry with small NPs of homogeneous morphology and controlled core/shell architecture in dispersion paves the way for future investigations – for instance, seeking different surface modification to retain these emissions in aqueous environments, leading to novel NIR nanothermometers for biomedical (and beyond) applications.

Experimental

Chemicals

Gadolinium oxide (Gd_2O_3, 99.999%), ytterbium oxide (Yb_2O_3, 99.998%), erbium oxide (Er_2O_3, 99.99%), thulium oxide (Tm_2O_3, 99.997%), and holmium oxide (Ho_2O_3, 99.995%) were purchased from Alfa Aesar. Trifluoroacetic acid (CF_3COOH, H-TFA, 98%), sodium trifluoroacetate (CF_3COONa, Na-TFA, 98%), oleic acid ($CH_3(CH_2)_7CH = CH(CH_2)_7COOH$, 90%), oleylamine ($CH_3(CH_2)_7CH = CH(CH_2)_7CH_2NH_2$, 70%), and 1-octadecene ($CH_3(CH_2)_{15}CH = CH_2$, 90%) were purchased from Sigma Aldrich. Ethanol (99%) was purchased from Commercial Alcohols. Acetone and hexane (analytical grade) were purchased from Fischer Chemicals. Toluene (99.8%) was purchased from Fisher Scientific. All chemicals were used as received.

Microwave-assisted synthesis of β-$NaGdF_4$:Yb^{3+},Er^{3+} and β-$NaGdF_4$:Ho^{3+},Tm^{3+} core NPs

The synthesis of β-$NaGdF_4$ NPs co-doped with 20 mol% of Yb^{3+} and 2 mol% of Er^{3+}, serving as cores in the final Er/Tm- and Er/Yb,Tm-CSS NP architectures, were obtained using the microwave-assisted thermal decomposition of lanthanide trifluoroacetate ([$Ln(TFA)_3$], Ln = Gd^{3+}, Yb^{3+}, Er^{3+}) and sodium trifluoroacetate (Na-TFA) precursors, following a procedure previously established by our group.[39] Briefly, for the synthesis of β-$NaGdF_4$ core NPs doped with 2 mol% of Er^{3+} and 20 mol% of Yb^{3+}, 0.625 mmol of [$Ln(TFA)_3$] were prepared mixing Gd_2O_3, Er_2O_3, and Yb_2O_3 in a 50 mL three-necked round-bottom flask, using the required mmol amounts outlined in Table S2. A 10 mL amount of a 1 : 1 TFA-to-H_2O mixture was added, and the slurry was refluxed at 95 °C until it became clear and dried at 60 °C overnight. Subsequently, 1.875 mmol of Na-TFA (3 : 1 Na^+-to-Ln^{3+} ion ratio) was added to the synthesized [$Ln(TFA)_3$] along with 2.5 mL of oleic acid, 2.5 mL of oleylamine, and 5 mL of 1-octadecene. This mixture was degassed at 120 °C under vacuum for 30 min. Subsequently, the degassed precursor solution was transferred to a 35 mL microwave vessel, purged with N_2 and tightly sealed. The vessel was inserted into a CEM Discovery SP microwave reactor. The precursor solution was heated to 280 °C for 1 s, followed by rapid cooling to 250 °C, the temperature at which the reaction mixture was held for 10 min, and subsequent cooling to 50 °C. Following the synthesis, the reaction mixture was washed with a 1 : 3 hexane-to-ethanol mixture and centrifuged at RCF = 6595*g* for 20 min. The product was then washed with a 1 : 3 toluene-to-acetone mixture and centrifuged using the same conditions. After purification, the NPs were dispersed and stored in 5 mL of toluene for further use. NaF as a potential by-product was removed by redispersing the NPs in 5 mL of ethanol prior to the addition of 5 mL of water, followed by precipitation *via* centrifugation. The obtained NPs were washed one more time with 10 mL of ethanol before being stored in 5 mL of toluene for further characterization. β-$NaGdF_4$ NPs doped with 1 mol% of Ho^{3+} and 10 or 15 mol% of Tm^{3+}, serving as cores in the Ho,Tm-CS NPs, were obtained following the same procedure, except that Gd_2O_3, Tm_2O_3, and Ho_2O_3 were used for the synthesis of the [$Ln(TFA)_3$] precursor. The required mmol amounts are outlined in Table S2.

Microwave-assisted growth of a shell (Er/Tm-, Er/Yb,Tm, and Ho,Tm-CS NPs)

For the growth of either an undoped β-$NaGdF_4$ shell (resulting in Ho,Tm-CS NPs), a Tm^{3+}-doped β-$NaGdF_4$ shell (resulting in Er/Tm-CS NPs) or an Yb^{3+}, Tm^{3+} co-doped β-$NaGdF_4$ shell (resulting in Er/Yb,Tm-CS NPs), the shell precursor ([$Ln(TFA)_3$], Ln = Gd^{3+}, Yb^{3+}, Tm^{3+}) was prepared as described above. Dopant concentrations and mmol amounts are provided in Table S2. 1.875 mmol of Na-TFA (3 : 1 Na^+-to-Ln^{3+} ratio), 4 mL of 1-octadecene and 5 mL of oleic acid were added to the shell precursor. The reaction mixture was degassed under vacuum at 120 °C for 30 min. The shell thickness was controlled by adjusting the ratio between the core NPs acting as seeds for shell growth and the shell precursor. More specifically, *ca.* 100 mg of the core NPs, prepared in the previous step, were used as seeds to grow the shell. The respective amount of core NPs was dispersed in 1 mL of octadecene (note: in contrast to the core synthesis, no oleylamine was used to grow the shell). Subsequently, this 1 mL of octadecene containing the core NPs and the 9 mL of the degassed shell

precursor solution were transferred to a 35 mL microwave vessel, purged with N_2, and tightly sealed. The vessel was inserted into a CEM Discover SP microwave reactor, and the mixture was heated to 250 °C and held for 10 min under stirring. The cooling and washing procedure as well as storage of the obtained core/shell NPs were as described above for the core NPs.

Microwave-assisted growth of a second shell (Er/Tm- and Er/Yb,Tm-CSS NPs)

The procedure to grow a second, outer shell of undoped $NaGdF_4$ was similar to that used for the synthesis of the CS-NPs described above, except that $[Gd(TFA)_3]$ was used as precursor. The shell precursor, 0.625 mmol of $[Gd(TFA)_3]$, was prepared as described above, using Gd^{3+} as sole lanthanide. 1.25 mmol of Na-TFA (2 : 1 Na^+-to-Gd^{3+} ratio), 4 mL of 1-octadecene and 5 mL of oleic acid were added to the precursor. The reaction mixture was degassed under vacuum at 120 °C for 30 min. The shell thickness was controlled by adjusting the ratio between the CS-NPs acting as seeds for shell growth and the shell precursor. More specifically, *ca.* 120 mg of the CS-NPs prepared in the previous step were used as seeds to grow the second shell. Subsequently, the 1 mL of octadecene containing the CS-NPs and the 9 mL of the degassed shell precursor solution were transferred to a 35 mL microwave vessel, purged with N_2, and tightly sealed. The vessel was inserted into a CEM Discover SP microwave reactor, and the mixture was heated to 250 °C and held for 10 min under stirring. The cooling and washing procedure as well as storage of the obtained CSS-NPs were as described above for the core NPs. Inductively coupled plasma mass spectrometry (ICP-MS) was performed to assess the actual *versus* nominal Ln^{3+} content in the resulting CSS-NPs. Results and a brief discussion are provided in the Table S3.

Characterization techniques

To determine the crystalline phase of the NPs, powder X-ray diffraction (XRD) analysis was performed using a Rigaku Ultima IV Diffractometer or a Bruker D8 Endeavor (Cu Kα, λ = 1.5401 Å), operating at 44 kV and 40 mA (step size: 0.02°, scan speed: 1° min^{-1}). Therefore, the NPs were deposited on a glass slide from their suspension. The morphology and size distribution of the obtained NPs were investigated by transmission electron microscopy (TEM, FEI Tecnai Spirit). The samples were dispersed on a Formvar/carbon film supported on a 300-mesh copper TEM grid. Size distributions (mean size ± standard deviation (SD)) of the samples were derived from TEM images using the software ImageJ and OriginPro. The respective size distributions were obtained analysing 200 particles per sample. Shell thickness was estimated based on the obtained diameters of core, core/shell, and core/shell/shell NPs.

The Ln^{3+} ion concentration in the samples was determined with an inductively coupled plasma mass spectrometer (ICP-MS, triple quadrupole 8800, Agilent). For sample preparation, 0.1 mL of the nanoparticle suspension was transferred to a digestion vessel and dried. Subsequently, 0.5 mL of concentrated HNO_3 was added, and the mixture was heated at 100 °C overnight to ensure complete digestion. After cooling, the digested sample was diluted to a final volume of 10 mL with ultrapure water prior to analysis. The ICP-MS was operated under the following conditions: RF Power at 1550 W, RF Matching at 1.80 V, sample depth at 10.0 mm, nebulizer gas flow at 1.01 L min^{-1}, no option gas, nebulizer pump speed at 0.10 rps, S/C temperature at 2 °C, dilution gas mode, and a makeup gas flow of 0.00 L min^{-1}. The ion optics parameters were set as follows: extract 1 at −16.8 V, extract 2 at −215.0 V, omega bias at −140 V, and omega lens at 10.0 V. These parameters ensured optimal sensitivity and reproducibility for lanthanide quantitation under MS/MS mode.

Investigation of the steady-state photoluminescence properties of the NPs in suspension (10 mg mL^{-1} in toluene) was carried out in a quartz cuvette (suitable spectral range from 200 to 2500 nm, 1 cm optical path) inserted into the Peltier temperature sample holder of a QuantaMaster 8075-21 spectrofluorometer from HORIBA. The spectrofluorometer was equipped with single grating emission monochromators, a red-extended photomultiplier detector R13456 PMT (185 to 980 nm), and a liquid nitrogen cooled InAs detector (1000 to 3450 nm). The NIR continuous excitation was performed using a 980 nm or 808 nm continuous-wave laser diode with a maximum power of 2 W. The power densities used to trigger NIR emission in toluene were 6.7 and 13.3 W cm^{-2} for 980 nm and 808 nm lasers, respectively, unless stated otherwise. The power density used to trigger the UC emission was 3.15 W cm^{-2} using the 980 nm laser diode. Laser-induced heating in toluene was determined using the 980 nm continuous-wave laser diode with laser power densities of 3.0, 5.3, and 6.7 W cm^{-2}. A type K thermocouple (stainless steel probe; Gain Express) connected to a type K handheld thermometer of 0.1 °C (Gain Express) was used for a contact measurement of the temperature inside of the cuvette. Power-dependent photoluminescence studies were performed using the same setup described above with different 980 nm laser power densities, *i.e.*, 3.0, 5.3, and 6.7 W cm^{-2}. For temperature-dependent photoluminescence measurements, the temperature was changed stepwise from 20 °C to 50 °C (following a heating regiment of 20, 30, 35, 40, 45, 50 °C), using the temperature-controlled Peltier sample holder with a liquid cooling system. At each step, the temperature was allowed to stabilize for 10 min prior to the measurement. Details about the analysis of the thermometric performance of the NPs are provided in the SI. For all the steady-state photoluminescence measurements, filters were placed in front of detectors. A long-pass 1025 nm filter was used for Er- and Tm-based samples, while a long-pass 1650 nm filter was used for Ho- and Tm-based samples to block the shorter Yb^{3+} emission at *ca.* 1030 nm, which might generate an artefact signal at 2060 nm. Integration time was set to 0.5 s, and the excitation and emission slit size was set to 30 nm for all measurements. Photoluminescence lifetimes were obtained by time-resolved spectroscopy, using the laser diodes in pulsed mode (laser power: 2 W). When monitoring

the Er^{3+}, Tm^{3+}, and Ho^{3+} NIR emission, the same filters as described for steady-state measurements were used. No filters were used when recording the decay profile of the Yb^{3+} emission at 940 nm. Lifetime values were obtained from (multi) exponential fits of the experimental data. Therefore, the average lifetime was calculated by eqn (1) using fitting parameters t and A (Fig. S4 and S11).

$$\tau_{\text{average}} = \frac{\sum (A_i \times t_i)}{\sum (A_i)} \quad (1)$$

Conflicts of interest

There are no conflicts to declare.

Data availability

The data supporting this article have been included as part of the SI. Supplementary information: Experimental details; additional structural analysis including XRD and TEM; ICP-MS analysis of CSS-NPs; time-dependent spectroscopy data (decay curves); laser-induced heating effects and power-dependent spectroscopy; upconversion emission spectra; additional temperature-dependent spectroscopy data. See DOI: **https://doi.org/10.1039/d5qi01571e**.

Any additional information can be obtained from the corresponding authors upon reasonable request.

Acknowledgements

The authors gratefully acknowledge the financial support provided by the University of Ottawa, the Canadian Foundation for Innovation (CFI), the Natural Sciences and Engineering Research Council of Canada (NSERC, RGPIN-2016-04830, RGPIN-2023-03985), and the National Research Council Canada (NRC, QSP 045-1). NL is thankful for financial support provided by China Scholarship Council (CSC).

References

1 B. Harrington, Z. Ye, L. Signor and A. D. Pickel, Luminescence thermometry beyond the biological realm, *ACS Nanosci. Au*, 2023, **4**, 30–61.
2 J. Zhou, B. Del Rosal, D. Jaque, S. Uchiyama and D. Jin, Advances and challenges for fluorescence nanothermometry, *Nat. Methods*, 2020, **17**, 967–980.
3 C. Bradac, S. F. Lim, H. C. Chang and I. Aharonovich, Optical nanoscale thermometry: From fundamental mechanisms to emerging practical applications, *Adv. Opt. Mater.*, 2020, **8**, 202000183.
4 B. del Rosal, E. Ximendes, U. Rocha and D. Jaque, In vivo luminescence nanothermometry: From materials to applications, *Adv. Opt. Mater.*, 2017, **5**, 1600508.
5 H. Suo, X. Zhao, Z. Zhang, Y. Wang, J. Sun, M. Jin and C. Guo, Rational design of ratiometric luminescence thermometry based on thermally coupled levels for bioapplications, *Laser Photonics Rev.*, 2020, **15**, 2000319.
6 Y. Zhao, X. Wang, Y. Zhang, Y. Li and X. Yao, Optical temperature sensing of up-conversion luminescent materials: Fundamentals and progress, *J. Alloys Compd.*, 2020, **817**, 152691.
7 C. D. Brites, P. P. Lima, N. J. Silva, A. Millan, V. S. Amaral, F. Palacio and L. D. Carlos, Thermometry at the nanoscale, *Nanoscale*, 2012, **4**, 4799–4829.
8 D. Jaque and F. Vetrone, Luminescence nanothermometry, *Nanoscale*, 2012, **4**, 4301–4326.
9 E. Hemmer, A. Benayas, F. Legare and F. Vetrone, Exploiting the biological windows: Current perspectives on fluorescent bioprobes emitting above 1000 nm, *Nanoscale Horiz.*, 2016, **1**, 168–184.
10 S. Golovynskyi, I. Golovynska, L. I. Stepanova, O. I. Datsenko, L. Liu, J. Qu and T. Y. Ohulchanskyy, Optical windows for head tissues in near-infrared and short-wave infrared regions: Approaching transcranial light applications, *J. Biophotonics*, 2018, **11**, 201800141.
11 L. A. Sordillo, Y. Pu, S. Pratavieira, Y. Budansky and R. R. Alfano, Deep optical imaging of tissue using the second and third near-infrared spectral windows, *J. Biomed. Opt.*, 2014, **19**, 056004.
12 X. Qi, C. Lee, B. Ursprung, A. Skripka, P. J. Schuck, E. M. Chan and B. E. Cohen, Short-wave infrared upconverting nanoparticles, *J. Am. Chem. Soc.*, 2024, **146**, 29292–29296.
13 Z. Feng, T. Tang, T. Wu, X. Yu, Y. Zhang, M. Wang, J. Zheng, Y. Ying, S. Chen, J. Zhou, X. Fan, D. Zhang, S. Li, M. Zhang and J. Qian, Perfecting and extending the near-infrared imaging window, *Light: Sci. Appl.*, 2021, **10**, 197.
14 A. Nexha, J. J. Carvajal, M. C. Pujol, F. Diaz and M. Aguilo, Lanthanide doped luminescence nanothermometers in the biological windows: strategies and applications, *Nanoscale*, 2021, **13**, 7913–7987.
15 Q. Wang, M. Liao, Q. Lin, M. Xiong, Z. Mu and F. Wu, A review on fluorescence intensity ratio thermometer based on rare-earth and transition metal ions doped inorganic luminescent materials, *J. Alloys Compd.*, 2021, **850**, 156744.
16 L. H. Fischer, G. S. Harms and O. S. Wolfbeis, Upconverting nanoparticles for nanoscale thermometry, *Angew. Chem., Int. Ed.*, 2011, **50**, 4546–4551.
17 M. Jia, Z. Fu, G. Liu, Z. Sun, P. Li, A. Zhang, F. Lin, B. Hou and G. Chen, NIR-II/III luminescence ratiometric nanothermometry with phonon-tuned sensitivity, *Adv. Opt. Mater.*, 2020, **8**, 1901173.
18 O. A. Savchuk, J. J. Carvajal, P. Haro-Gonzalez, M. Aguiló and F. Díaz, Luminescent nanothermometry using short-wavelength infrared light, *J. Alloys Compd.*, 2018, **746**, 710–719.
19 O. A. Savchuk, J. J. Carvajal, C. D. S. Brites, L. D. Carlos, M. Aguilo and F. Diaz, Upconversion thermometry: A new tool to measure the thermal resistance of nanoparticles, *Nanoscale*, 2018, **10**, 6602–6610.

20 S. Goderski, M. Runowski, P. Wozny, V. Lavin and S. Lis, Lanthanide upconverted luminescence for simultaneous contactless optical thermometry and manometry–sensing under extreme conditions of pressure and temperature, *ACS Appl. Mater. Interfaces*, 2020, **12**, 40475–40485.

21 U. Rocha, W. F. Silva, I. Guedes, A. Benayas, L. M. Maestro, E. Bovero, F. C. J. M. van Veggel, J. A. G. Sole and D. Jaque, Subtissue thermal sensing based on neodymium-doped LaF_3 nanoparticles, *ACS Nano*, 2013, **7**, 1188–1199.

22 C. Hazra, A. Skripka, S. J. L. Ribeiro and F. Vetrone, Erbium single-band nanothermometry in the third biological imaging window: Potential and limitations, *Adv. Opt. Mater.*, 2020, **8**, 2001178.

23 A. Skripka, A. Benayas, R. Marin, P. Canton, E. Hemmer and F. Vetrone, Double rare-earth nanothermometer in aqueous media: Opening the third optical transparency window to temperature sensing, *Nanoscale*, 2017, **9**, 3079–3085.

24 A. Skripka, A. Morinvil, M. Matulionyte, T. Cheng and F. Vetrone, Advancing neodymium single-band nanothermometry, *Nanoscale*, 2019, **11**, 11322–11330.

25 S. Balabhadra, M. L. Debasu, C. D. Brites, L. A. Nunes, O. L. Malta, J. Rocha, M. Bettinelli and L. D. Carlos, Boosting the sensitivity of Nd^{3+}-based luminescent nanothermometers, *Nanoscale*, 2015, **7**, 17261–17267.

26 W. Xu, D. Zhao, X. Zhu, L. Zheng, Z. Zhang and W. Cao, NIR to NIR luminescence thermometry in core/multishells-structured nanoparticles operating in the biological window, *J. Lumin.*, 2020, **225**, 117358.

27 M. Back, E. Casagrande, E. Trave, D. Cristofori, E. Ambrosi, F. Dallo, M. Roman, J. Ueda, J. Xu, S. Tanabe, A. Benedetti and P. Riello, Confined-melting-assisted synthesis of bismuth silicate glass-ceramic nanoparticles: formation and optical thermometry investigation, *ACS Appl. Mater. Interfaces*, 2020, **12**, 55195–55204.

28 M. Suta, Z. Antic, V. Ethordevic, S. Kuzman, M. D. Dramicanin and A. Meijerink, Making Nd^{3+} a sensitive luminescent thermometer for physiological temperatures—an Account of pitfalls in Boltzmann thermometry, *Nanomaterials*, 2020, **10**, 10030543.

29 Y. Cheng, Y. Gao, H. Lin, F. Huang and Y. Wang, Strategy design for ratiometric luminescence thermometry: Circumventing the limitation of thermally coupled levels, *J. Mater. Chem. C*, 2018, **6**, 7462–7478.

30 M. Runowski, S. Goderski, D. Przybylska, T. Grzyb, S. Lis and I. R. Martín, Sr_2LuF_7:Yb^{3+}–Ho^{3+}–Er^{3+} upconverting nanoparticles as luminescent thermometers in the first, second, and third biological windows, *ACS Appl. Nano Mater.*, 2020, **3**, 6406–6415.

31 A. Puccini, N. Liu and E. Hemmer, Praseodymium-doped nanoparticles: Candidates for near-infrared-ii double- and single-band nanothermometry, *ACS Mater. Lett.*, 2024, **6**, 1327–1337.

32 E. Casagrande, M. Back, D. Cristofori, J. Ueda, S. Tanabe, S. Palazzolo, F. Rizzolio, V. Canzonieri, E. Trave and P. Riello, Upconversion-mediated Boltzmann thermometry in double-layered Bi_2SiO_5:Yb^{3+},Tm^{3+}@SiO_2 hollow nanoparticles, *J. Mater. Chem. C*, 2020, **8**, 7828–7836.

33 H. Wang, F. Li, P. Wang, X. Fan, L. Meng, J. Zhang, M. Zhang, Y. Zheng, N. Kong and X. Zhu, Enhancing thermal sensitivity of NIR-IIb lanthanide nanothermometers for in vivo luminescence nanothermometry via erbium sublattice-mediated energy recycling, *Adv. Funct. Mater.*, 2025, e06126.

34 A. Bednarkiewicz, L. Marciniak, L. D. Carlos and D. Jaque, Standardizing luminescence nanothermometry for biomedical applications, *Nanoscale*, 2020, **12**, 14405–14421.

35 L. Labrador-Paez, M. Pedroni, A. Speghini, J. Garcia-Sole, P. Haro-Gonzalez and D. Jaque, Reliability of rare-earth-doped infrared luminescent nanothermometers, *Nanoscale*, 2018, **10**, 22319–22328.

36 A. C. C. Soares, T. O. Sales, E. C. Ximendes, D. Jaque and C. Jacinto, Lanthanide doped nanoparticles for reliable and precise luminescence nanothermometry in the third biological window, *Nanoscale Adv.*, 2023, **5**, 3664–3670.

37 A. Nexha, J. J. Carvajal, M. C. Pujol, F. Díaz and M. Aguiló, Short-wavelength infrared self-assessed photothermal agents based on Ho,Tm:$KLu(WO_4)_2$ nanocrystals operating in the third biological window (1.45–1.96 μm wavelength range), *J. Mater. Chem. C*, 2020, **8**, 180–191.

38 J. Li, Y. Guan, G. Xin, L. Wang, L. Zhang, S. Zhang and L. Liu, Er/Tm based NIR-III dual-band emissive bioprobe for imaging and temperature readout, *Opt. Commun.*, 2022, **525**, 128870.

39 N. Liu, C. Homann, S. Morfin, M. S. Kesanakurti, N. D. Calvert, A. J. Shuhendler, T. Al and E. Hemmer, Core–multi-shell design: Unlocking multimodal capabilities in lanthanide-based nanoparticles as upconverting, T_2-weighted MRI and CT probes, *Nanoscale*, 2023, **15**, 19546–19556.

40 F. Ren, H. Huang, H. Yang, B. Xia, Z. Ma, Y. Zhang, F. Wu, C. Li, T. He and Q. Wang, Tailoring near-infrared-IIb fluorescence of Thulium(III) by nanocrystal structure engineering, *Nano Lett.*, 2023, **23**, 10058–10065.

41 M. Quintanilla, E. Hemmer, J. Marques-Hueso, S. Rohani, G. Lucchini, M. Wang, R. R. Zamani, V. Roddatis, A. Speghini, B. S. Richards and F. Vetrone, Cubic versus hexagonal – phase, size and morphology effects on the photoluminescence quantum yield of $NaGdF_4$:Er^{3+}/Yb^{3+} upconverting nanoparticles, *Nanoscale*, 2022, **14**, 1492–1504.

42 S. Bhuckory, E. Hemmer, Y. T. Wu, A. Yahia-Ammar, F. Vetrone and N. Hildebrandt, Core or shell? Er^{3+} FRET donors in upconversion nanoparticles, *Eur. J. Inorg. Chem.*, 2017, 5186–5195.

43 N. J. Johnson, S. He, S. Diao, E. M. Chan, H. Dai and A. Almutairi, Direct evidence for coupled surface and concentration quenching dynamics in lanthanide-doped nanocrystals, *J. Am. Chem. Soc.*, 2017, **139**, 3275–3282.

44 Y. Wang, B. Chen and F. Wang, Overcoming thermal quenching in upconversion nanoparticles, *Nanoscale*, 2021, **13**, 3454–3462.
45 T. Miyakawa and D. L. Dexter, Phonon sidebands, multiphonon relaxation of excited states, and phonon-assisted energy transfer between ions in solids, *Phys. Rev. B*, 1970, **1**, 2961–2969.
46 C. D. S. Brites, A. Millán and L. D. Carlos, Lanthanides in luminescent thermometry, in *Handbook on the Physics and Chemistry of Rare Earths*, ed. J. C. G. Bunzli and V. K. Pecharsky, Elsevier Science, B. V., Amsterdam, 2016, pp. 339.
47 A. Puccini, N. Liu and E. Hemmer, Lanthanide-based nanomaterials for temperature sensing in the near-infrared spectral region: Illuminating progress and challenges, *Nanoscale*, 2024, **16**, 10975–10993.
48 S. A. Payne, L. K. Smith, W. L. Kway, J. B. Tassano and W. F. Krupke, The mechanism of Tm to Ho energy transfer in $LiYF_4$, *J. Phys.: Condens. Matter*, 1992, **4**, 8525–8542.
49 Y. F. Li, Y. Z. Wang, B. Q. Yao and Y. M. Liu, Upconversion spectrum of Tm,Ho:$GdVO_4$ pumped by pulse and CW laser at 800 nm, *Laser Phys. Lett.*, 2008, **5**, 597–599.
50 A. Nexha, J. J. Carvajal, M. C. Pujol, F. Díaz and M. Aguiló, Synthesis of monoclinic Ho,Tm:$KLu(WO_4)_2$ microrods with high photothermal conversion efficiency via a thermal decomposition-assisted method, *J. Mater. Chem. C*, 2021, **9**, 2024–2036.
51 F. Xu, L. Zheng, M. Li, P. Zhou, J. Shi and Y. Pu, Temperature-dependent photoluminescence spectra of Er-Tm codoped calcium boroaluminate glasses, *Appl. Opt.*, 2012, **51**, 1115–1121.